https://doi.org/10.5194/wes-2024-107
Preprint. Discussion started: 10 September 2024
© Author(s) 2024. CC BY 4.0 License.

WIND ENERGY SCIENCE DISCUSSIONS

Direct integration of non-axisymmetric Gaussian wind-turbine wake including yaw and wind-veer effects

Karim Ali[1], Pablo Ouro[1], and Tim Stallard[1]

[1]School of Engineering, University of Manchester, Manchester, M13 9PL, UK

Correspondence: Pablo Ouro (pablo.ouro@manchester.ac.uk)

Abstract. The performance of a wind farm is significantly influenced by turbine-wake interactions. These interactions are typically quantified for each turbine by evaluating its rotor-averaged wind speed, which is impacted by upstream wakes, using numerical methods that involve discrete points across the rotor disk. Although various point distributions exist in the literature, we introduce an analytical expression for integrating a Gaussian wake over a circular disk, which accounts for wake stretching and shearing resulting from upstream turbine yaw and wind veer. This expression is versatile, accommodating any lateral offset and hub-height difference between the wake source (upstream turbines) and the target turbine. Validation against numerical evaluations of the rotor-averaged deficit at various downstream locations from the wake source demonstrates excellent agreement. Furthermore, the analytical expression is shown to be compatible with multiple wake superposition models. The presented solution is differentiable, providing a foundation for deriving mathematical expressions for the gradients of a turbine's power generation concerning its location within a farm and/or the operational conditions of upstream turbines. This capability is particularly advantageous for optimization-based applications.

1 Introduction

The widespread deployment of wind farms necessitates the use of accurate and efficient computational tools for preliminary design and optimisation (Veers et al., 2023). While Computational Fluid Dynamics (CFD) methods such as Large-Eddy Simulation (LES) and Reynolds-Averaged Navier-Stokes (RANS) offer detailed insights into turbine loading and wake dynamics, they are often too computationally intensive for preliminary wind-farm design and layout optimisation (Maas and Raasch, 2022). Mesoscale models require less computational power and have been employed to examine the large-scale interactions between wind turbine wakes and the turbulent atmospheric boundary layer, though they lack the detailed wake resolution provided by RANS and LES models (Fitch et al., 2012; Ali et al., 2023). Conversely, engineering wake models are comparatively faster and are extensively used in various wind-energy applications, including wind-farm layout optimisation and control (Hou et al., 2016; Bay et al., 2018; Shapiro et al., 2022). Engineering wake models, which assume that a turbine's wake is self similar, represent the wake using a streamwise scaling deficit function and a shape function to describe the deficit distribution perpendicular to the streamwise direction. Various shape functions have been proposed, including top-hat profiles (Jensen, 1983), Gaussian profiles (Bastankhah and Porté-Agel, 2014), double-Gaussian profiles (Keane et al., 2016), super-Gaussian profiles (Blondel and Cathelain, 2020), and profiles based on the diffusion of a passive scalar (Cheng and Porté-Agel, 2018;

https://doi.org/10.5194/wes-2024-107
Preprint. Discussion started: 10 September 2024
© Author(s) 2024. CC BY 4.0 License.

Ali et al., 2024c). Among these, the Gaussian wake profile is widely adopted particularly for distances comparable to a typical turbine spacing within a wind farm.

To assess the impact of an upstream turbine's wake on the onset flow of a downstream rotor, such as required to estimate energy-yield reduction due to wake effects, numerical methods often average upstream deficits calculated at multiple control points across the rotor disk of the considered turbine. The number and distribution of these averaging points vary in the literature. Allaerts and Meyers (2019) employed a 16-point quadrature based on Holoborodko (2011) in their analysis of wind-farm blockage and induced gravity waves, whereas Stipa et al. (2024) utilised a cross-like distribution of 16 averaging points to enhance radial resolution across the rotor. Stanley and Ning (2019) used 100 equally-spread averaging points for the evaluation of the rotor-averaged deficit. Other studies proposed uniform radial and azimuthal distribution of averaging points across the rotor within the context of farm layout optimisation and control (Li et al., 2022; Ling et al., 2024).

Uncertainties can arise from the number, distribution, and averaging weights of the control points, especially when the shape of the upstream wake deviates from the axisymmetric form due to, for instance, wind-veer effects. Rather than numerical averaging, Ali et al. (2024a) developed an analytical expression for the circular-disk integration of an axisymmetric Gaussian function depicting the wake of an upstream turbine. Their formulation is applicable to any lateral offset between the upstream turbine (wake source) and the considered turbine, but assumes that the upstream wake is axisymmetric and that both the upstream and downstream turbines have the same hub-height. Typically, turbines can be yawed relative to their onset wind yielding wakes that are not axisymmetric but of elliptic shape (Bastankhah and Porté-Agel, 2016). Additionally, wind-veer effects can cause planar shearing of the wake shape through stretching the wake elliptic contours and rotating its major axes (see Fig. 1 later in the article), resulting in further deviation from the axisymmetric wake shape (Abkar et al., 2018). Furthermore, onshore wind farms often have turbines with different hub heights due to non-flat terrain, and offshore wind farms may have turbines of varying hub heights and diameters operating in close proximity.

In this study, we extend the analytical solution proposed by Ali et al. (2024a) by generalising the assumed upstream wake shape to include non-symmetry due to the yawing of the wake source, wind-veer effects, and different hub-heights between the wake source and target turbine. Although the primary focus is on wind-turbine wakes, the proposed expression is also applicable to tidal-stream turbines and can be extended to vertical-axis turbines (both wind and tidal) due to the relevance of similar Gaussian wake profiles (e.g., Stallard et al., 2015; Ouro and Lazennec, 2021). The rest of this paper is structured as follows. Section 2 presents the generalised analytical expression for the rotor-averaged deficit, which is validated against numerical solutions for a single upstream wake in section 3.1 and for multiple upstream wakes in section 3.2. The key findings of this paper are discussed in more detail in section 4 with a focus on compatibility with different wake superposition models and applicability to yawed turbines, with a summary in section 5. Appendices A–D contain mathematical details on the derivation of the generalised rotor-averaged deficit, whereas the distribution of the averaging points used in the validation presented in section 3 are detailed in Appendix E. Further mathematical manipulations regarding wake superposition is included in Appendix F following the discussion in section 4.

https://doi.org/10.5194/wes-2024-107
Preprint. Discussion started: 10 September 2024
© Author(s) 2024. CC BY 4.0 License.

2 Analytical evaluation of the rotor-averaged wind-speed deficit

In this study, we seek to analytically evaluate the rotor-averaged deficit of a turbine operating within an upstream Gaussian wake whose shape and center are defined. For simplicity, the expression for the rotor-averaged deficit is derived for a single upstream wake, but extension to multiple upstream wakes is straightforward (section 3.2).

2.1 Problem definition

The normalised wind-speed deficit (W) due to the wake of an upstream turbine impacted by a constant transverse wind (causing wind veer) can be expressed as (Bastankhah and Porté-Agel, 2016; Abkar et al., 2018)

$$W = 1 - \frac{u}{\tilde{u}_n} = C(x)\, e^{-(y_n+\omega z_n)^2/(2\sigma_y^2)} e^{-z_n^2/(2\sigma_z^2)}, \tag{1}$$

where u is the streamwise wind speed, $\tilde{u}_n$ is the rotor-averaged wind speed of the upstream turbine (wake source), C is a streamwise scaling function, and x is the streamwise distance between the two turbines. The variables y_n and z_n are the lateral and vertical coordinates respectively, with an origin at the wake center, and $\omega = \Delta\alpha(x/D_n)$ is a wind-veer coefficient with $\Delta\alpha$ being the difference in wind direction across the top and bottom tips of the upstream turbine (wake source) whose diameter is D_n. The variables σ_y and σ_z are the wake standard deviations in the y_n and z_n directions, respectively. Figure 1 illustrates a schematic of an upstream turbine (of radius R_n) whose wake center is deflected horizontally by a distance d. The Cartesian coordinates y_n–z_n are placed at the center of the wake in the plane containing the considered turbine which is at a streamwise distance x from the wake source. The considered turbine is located at (Δ_y, Δ_z) with respect to the wake center with polar coordinates ρ and δ. The Cartesian axes y–z are placed at the center of the considered turbine which is of radius R. The lateral offset ρ is measured from the center of the wake, which is assumed to be known from wake deflection models (e.g., Bastankhah and Porté-Agel, 2016; Qian and Ishihara, 2018; Snaiki and Makki, 2024).

For a yawed upstream turbine, the wake standard deviations σ_y and σ_z are not equal, resulting in elliptic wake contours rather than circular contours in the specific case of axisymmetric wake. We define the eccentricity ξ of the wake elliptic contours due to having non-equal σ_y and σ_z as $\xi^2 = 1 - (\sigma_y/\sigma_z)^2$. Here, it is assumed that $\sigma_y \le \sigma_z$, which is the typical case for yawed horizontal-axis wind turbines. However, it is noted that where relevant, scenarios with $\sigma_y > \sigma_z$ can be obtained by a rotation of axes. In the following calculations, σ_z will be denoted as σ and hence $\sigma_y = \sigma\sqrt{1-\xi^2}$. A typical range for the eccentricity ξ can be identified using the empirical expressions for σ_y and σ_z for a yawed upstream turbine at an angle γ_n

$$\sigma_z = \sigma = k_z^* x + \sigma_{z_0} D_n, \qquad \text{and} \qquad \sigma_y = \sigma\sqrt{1-\xi^2} = k_y^* x + \sigma_{z_0} D_n \cos\gamma_n, \tag{2}$$

where k_z^* and k_y^* are the rates of wake expansion in the z_n and y_n directions respectively, and $\sigma_{z_0} \approx 1/\sqrt{8}$ is an initial wake standard deviation (Bastankhah and Porté-Agel, 2016). For simplicity we assume that $k_z^* = k_y^* = k^*$, and hence

$$\xi^2 \approx 1 - \left(\frac{k^* x/\sigma_{z_0} + \cos\gamma_n}{k^* x/\sigma_{z_0} + 1}\right)^2 \le 1 - \cos^2\gamma_n. \tag{3}$$

The typical range of a turbine yaw angle is less than 30° (Zong and Porté-Agel, 2021), and hence the eccentricity of the wake elliptic contours $\xi < 0.5$ for a typical inter-turbine spacing.

https://doi.org/10.5194/wes-2024-107
Preprint. Discussion started: 10 September 2024
© Author(s) 2024. CC BY 4.0 License.

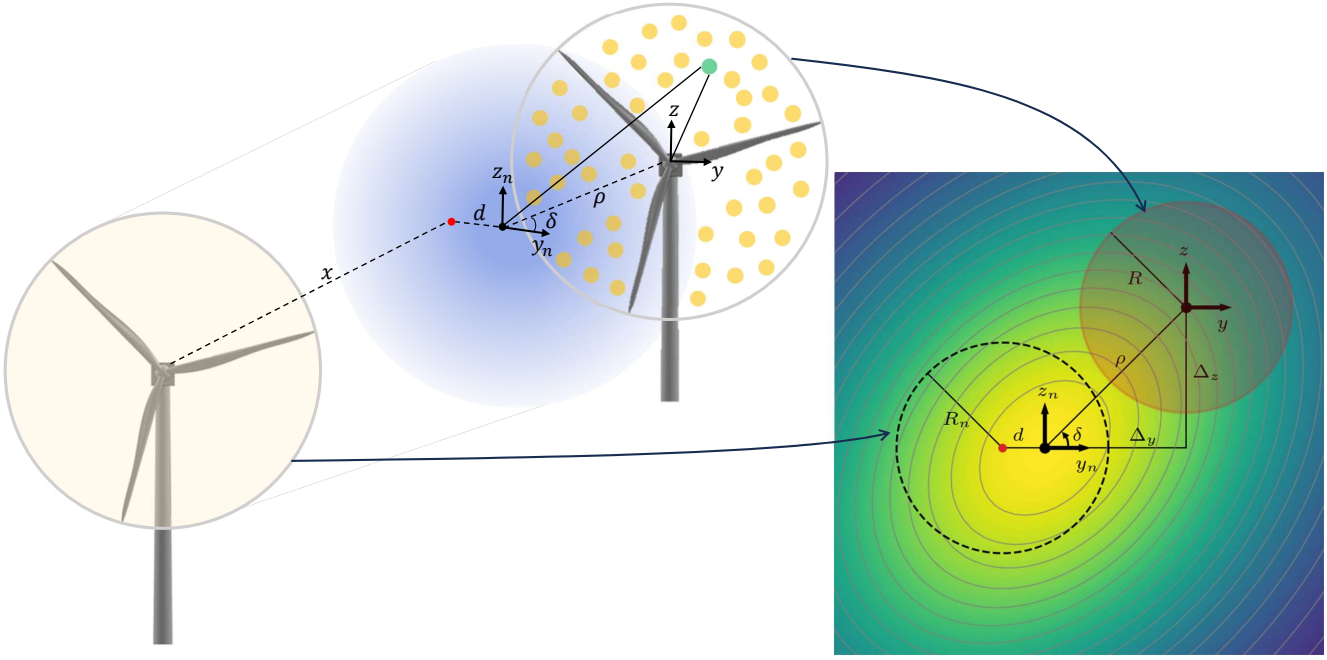

Figure 1. Schematic contours of the normalised wind-speed deficit W due to an upstream wake. The center of the wake (origin of the axes y_n–z_n) is deflected horizontally by a distance d from its source center (upstream turbine denoted by the dashed circle), and the considered turbine is offset from the wake center by a radial distance ρ and an angle δ. The axes y–z are placed at the center of the considered turbine and are located at (Δ_y, Δ_z) with respect to the wake axes y_n–z_n. The shown elliptic contours have an eccentricity $\xi = 0.4$ and a veer-coefficient $\omega = -0.3$, with definitions of ξ and ω provided in the main text. The upstream turbine (wake source) has a radius R_n and the considered turbine has a radius R. The yellow dots on the rotor disk of the considered turbine (downstream turbine) are exemplary of the averaging points that are used to numerically evaluate the rotor-averaged wind speed.

https://doi.org/10.5194/wes-2024-107
Preprint. Discussion started: 10 September 2024
© Author(s) 2024. CC BY 4.0 License.

A Gaussian wake description, as given in Eq. 1, assumes a neutral atmospheric boundary layer for which the typical magnitude of wind veer is approximately of the order 0.03°/m (Walter et al., 2009; Gao et al., 2021). Hence, for large wind turbine (diameter ~ 220 m) operating in a neutral boundary layer, the difference in wind direction across its top and bottom tips is less than approximately 7°. While stable stratification and/or complex terrain can intensify wind veer, we limit our calculations to neutral boundary layers with moderate wind veer (i.e., $\Delta\alpha \lesssim 7°$). The angle δ corresponds to the difference in hub-height between the upstream turbine (wake source) and the considered downstream turbine. In a typical wind farm, all turbines have the same hub-height, making $\delta = 0$ (or π). However, our calculations consider δ as a variable to accommodate cases with differing hub heights, such as adjacent wind farms or non-uniform terrain.

To summarise, the objective is to determine the rotor-averaged deficit of a turbine of radius R operating within an upstream Gaussian wake defined by the standard deviation σ, the wake eccentricity ξ, the veer coefficient ω, and the streamwise scaling function C, by performing a surface integration of Eq. 1 over the rotor disk of the considered turbine (shaded circle in Fig. 1), which is offset from wake center by the radial distance ρ and the angle δ. We assume that the rotor disk of the considered turbine is normal to the free-stream direction implying that σ, ξ, ω, and C, are constants across the rotor disk of the considered turbine.

2.2 Generalised rotor-averaged deficit of a Gaussian wake

The presented derivation in this section is a generalisation to the solution by Ali et al. (2024a) who solved a similar problem but for an axisymmetric wake (i.e., $\xi = \omega = 0$) and for two turbines of the same hub-height (i.e., $\delta = 0$). From Eq. 1, the rotor-averaged deficit $\tilde{W}$ of the considered turbine is

$$\tilde{W} = \frac{C}{\pi R^2} \int_0^R \int_0^{2\pi} r e^{-(y_n+\omega z_n)^2/(2\sigma_y^2)} e^{-z_n^2/(2\sigma_z^2)} \, d\theta \, dr, \tag{4}$$

where r, θ are the polar coordinates of the axes y–z placed at the center of the considered turbine (Fig. 1). The coordinates y_n–z_n (of the wake center) and y–z can be related using $y_n = y + \Delta_y$ and $z_n = z + \Delta_z$ (Fig. 1). These relations, along with $\langle y, z\rangle = r\langle \cos\theta, \sin\theta\rangle$ and $\langle \Delta_y, \Delta_z\rangle = \rho\langle \cos\delta, \sin\delta\rangle$, where $\langle t_1, t_2\rangle$ means t_1 or t_2, can be used to re-write Eq. 4 in the r–θ coordinates as (see Appendix A for derivation)

$$\tilde{W} = C e^{-\rho^2/(2\sigma_*^2)} e^{-\rho^2\cos(2\delta-\phi_{\rm ns})/(2\sigma_{\rm ns}^2)} \underbrace{\int_0^1 \eta e^{-\eta^2 R^2/(2\sigma_*^2)} \underbrace{\int_0^{2\pi} \frac{1}{\pi} e^{-\eta^2 R^2 \cos(2\theta-\phi_{\rm ns})/(2\sigma_{\rm ns}^2)} e^{-\eta R\rho\cos(\theta-\phi_{\rm s})/\sigma_{\rm s}^2} \, d\theta}_{M_\theta} \, d\eta}_{M_\eta}, \tag{5}$$

where $\eta = r/R$. In Eq. 5, three new length scales are introduced: σ_*, $\sigma_{\rm ns}$, and $\sigma_{\rm s}$ along with two new angles: $\phi_{\rm ns}$ and $\phi_{\rm s}$, which are defined in terms of the wake standard deviation σ, the eccentricity ξ, the veer coefficient ω, and the angle δ as

$$\sigma_*^2 = \frac{2\sigma^2(1-\xi^2)}{2+\omega^2-\xi^2}, \quad \sigma_{\rm ns}^2 = \frac{2\sigma^2(1-\xi^2)}{\sqrt{(\omega^2-\xi^2)^2+4\omega^2}}, \quad \sigma_{\rm s}^2 = \frac{\sigma^2\left(1-\xi^2\right)\cos\phi_{\rm s}}{\cos\delta+\omega\sin\delta}, \quad \tan\phi_{\rm ns} = \frac{2\omega}{\xi^2-\omega^2}, \quad \tan\phi_{\rm s} = \omega + \frac{\left(1-\xi^2\right)\tan\delta}{1+\omega\tan\delta}.$$

https://doi.org/10.5194/wes-2024-107
Preprint. Discussion started: 10 September 2024
© Author(s) 2024. CC BY 4.0 License.

(6)

The subscript "ns" refers to wake non-symmetry. In case of an axisymmetric wake (i.e., $\omega = \xi = 0$), we have $\sigma_{\text{ns}}^{-1} = 0$ and hence its corresponding exponential terms in Eq. 5 vanish. Also, when the wake is axisymmetric we have $\sigma_* = \sigma_{\text{s}} = \sigma$, and $\phi_{\text{s}} = \delta$. The solution to the integral M_θ in Eq. 5 is (see derivation in Appendix B)

$$M_\theta = 2I_0\left(\frac{\eta R\rho}{\sigma_{\text{s}}^2}\right) I_0\left(\frac{\eta^2 R^2}{2\sigma_{\text{ns}}^2}\right) + 4\sum_{\nu\geq 1}(-1)^\nu \cos(\nu\phi)\, I_{2\nu}\left(\frac{\eta R\rho}{\sigma_{\text{s}}^2}\right) I_\nu\left(\frac{\eta^2 R^2}{2\sigma_{\text{ns}}^2}\right), \tag{7}$$

where I_ν is the modified Bessel function of the first kind and order ν, and $\phi = 2\phi_{\text{s}} - \phi_{\text{ns}}$. By employing Eq. 7, the solution of the integral M_η in Eq. 5 is (Appendix C)

$$M_\eta \approx 2\mu_0\left(1 + 2\mathcal{P}_{\text{ns}}\right) - \frac{4\sigma_*^2}{R^2} e^{-R^2/(2\sigma_*^2)} \mathcal{P}_{\text{ns}}\left[\frac{\lambda}{\rho} I_1\left(\frac{R\rho}{\sigma_{\text{s}}^2}\right) + \frac{\lambda^2}{\rho^2} I_2\left(\frac{R\rho}{\sigma_{\text{s}}^2}\right)\right], \tag{8}$$

where $\mathcal{P}_{\text{ns}} = \cos(\chi_{\text{ns}}^2 \sin\phi) e^{-\chi_{\text{ns}}^2 \cos\phi} - 1$, $\chi_{\text{ns}} = \rho\sigma_*^2/(2\sigma_{\text{ns}}\sigma_{\text{s}}^2)$, and $\lambda = R\sigma_{\text{s}}^2/\sigma_*^2$. In Eq. 8, μ_0 is

$$\mu_0 = \int_0^1 \eta e^{-\eta^2 R^2/(2\sigma_*^2)} I_0\left(\frac{\eta R\rho}{\sigma_{\text{s}}^2}\right) d\eta. \tag{9}$$

In the case of an axisymmetric wake ($\sigma_{\text{ns}}^{-1} = 0$), we have $\chi_{\text{ns}} = \mathcal{P}_{\text{ns}} = 0$, and Eq. 8 simplifies to $M_\eta \approx 2\mu_0$. Therefore, Eq. 8 indicates that the solution of the non-axisymmetric wake (Eq. 1) is a perturbation (second term in Eq. 8) to scaled axisymmetric solution (scaled by $1 + 2\mathcal{P}_{\text{ns}}$). Equation 8 contains terms in the form $I_\nu(R\rho/\sigma_{\text{s}}^2)/\rho$, which has a finite value when there is no lateral offset between the wake source and the considered turbine ($\rho = 0$) as $\lim_{\rho\to 0} I_\nu(R\rho/\sigma_{\text{s}}^2)/\rho = 1/(2^\nu \nu!)$. Nonetheless, when $\rho = 0$, $\mathcal{P}_{\text{ns}} = 0$ similar to the axisymmetric solution. This results from the simplifying assumption made in Appendix C to solve for M_η where the terms $I_\nu\left(\eta^2 R^2/(2\sigma_{\text{ns}}^2)\right)$ were approximated by $(\eta^2 R^2/(4\sigma_{\text{ns}}^2))^\nu/\nu!$ under the assumption that the argument of the modified Bessel function is small (following the limits on the wind veer discussed in section 2.1), and hence $I_0\left(\eta^2 R^2/(2\sigma_{\text{ns}}^2)\right) \sim 1$ was employed. This means that the stretching and shearing acting on the wake are assumed to have minimal effect on the wake shape close to the wake center and are more profound far from the wake center. We will show in section 3.1, both numerically and analytically, that this assumption is acceptable for moderate values of wind veer by monitoring the average value (within the range $0 \leq \eta \leq 1$) of the argument of the modified Bessel function $\kappa = R^2/(6\sigma_{\text{ns}}^2)$. The solution of the integral μ_0 can be obtained by generalising the solution introduced by Ali et al. (2024a) based on Rosenheinrich (2017)

$$\mu_0 = \frac{\sigma_*^2}{R^2} e^{-R^2/(2\sigma_*^2)} \Psi(R, \rho, \sigma_{\text{s}}, \sigma_*), \tag{10}$$

where

$$\Psi(R, \rho, \sigma_{\text{s}}, \sigma_*) = I_0\left(\frac{R\rho}{\sigma_{\text{s}}^2}\right) \sum_{k\geq 1}\left[\left(\frac{R^2}{2\sigma_*^2}\right)^k f_k(\tau^2)\right] - \frac{R\rho}{\sigma_{\text{s}}^2} I_1\left(\frac{R\rho}{\sigma_{\text{s}}^2}\right) \sum_{k\geq 1}\left[\left(\frac{R^2}{2\sigma_*^2}\right)^k g_k(\tau^2)\right], \tag{11}$$

and $\tau = \rho\sigma_*/\sigma_{\text{s}}^2$. The coefficients f_k and g_k follow

$$f_k(\tau) = \frac{f_{k-1}(\tau) + \tau g_{k-1}(\tau)}{k}, \quad g_k(\tau) = \frac{f_k(\tau) + 2g_{k-1}(\tau)}{2k}, \tag{12}$$

https://doi.org/10.5194/wes-2024-107
Preprint. Discussion started: 10 September 2024
© Author(s) 2024. CC BY 4.0 License.

with $f_0 = 1$, $g_0 = 0$. The recursions in Eq. 12 converge rapidly within 6–10 iterations of simple algebraic calculations. From Eq. 5, the final form of the rotor-averaged deficit is

$$\tilde{W} \approx 2Ce^{-\rho^2/(2\hat{\sigma}^2)} \left(\mu_0 \left(1 + 2\mathcal{P}_{\text{ns}}\right) - \frac{2\sigma_*^2}{R^2} e^{-R^2/(2\sigma_*^2)} \mathcal{P}_{\text{ns}} \left[\frac{\lambda}{\rho} I_1 \left(\frac{R\rho}{\sigma_{\text{s}}^2} \right) + \frac{\lambda^2}{\rho^2} I_2 \left(\frac{R\rho}{\sigma_{\text{s}}^2} \right) \right] \right), \tag{13}$$

where $\hat{\sigma}^{-2} = \sigma_*^{-2} + \sigma_{\text{ns}}^{-2} \cos\left(2\delta - \phi_{\text{ns}}\right)$. Equation 13 was implemented in Python and available from Ali et al. (2024b).

3 Validation

In this section, the developed analytical solution (Eq. 13) is validated against numerical evaluation of the rotor-averaged deficit for the case of a single upstream wake (section 3.1), and for the case of multiple upstream wakes (section 3.2). The numerical reference against which Eq. 13 is validated is 2000 averaging points uniformly distributed across the rotor disk following a sunflower distribution (details in Appendix E) as shown in Fig. E1.

3.1 Single upstream wake

We consider the non-axisymmetric Gaussian wake of a wind turbine (Eq. 1) and evaluate the rotor-averaged deficit of a downstream turbine due to this wake at various downstream locations relative to the wake source. The upstream turbine, acting as the wake source, operates at a yaw angle $\gamma_n = 20°$ with combinations of low ($C_t = 0.4$) and high ($C_t = 0.8$) thrust coefficients and low ($T_i = 5\%$) and high ($T_i = 12\%$) free-stream turbulence intensities. As discussed in section 2.1, the difference in wind direction across the top and bottom tips of the upstream turbine is assumed to be 7°, corresponding to a moderate wind veer acting on a large turbine (diameter $\sim$ 220 m), and hence the veer coefficient $\omega \approx 0.122x/D_n$. For simplicity, hereafter the subscript n for the radius and diameter of the upstream turbine is dropped by assuming that the upstream and downstream turbines are of the same size, which does not impact the generality of Eq. 13. At each downstream location from the wake source, the wake eccentricity ξ can be obtained from Eq. 3 using the empirical expression $k^* = 0.003678 + 0.3837T_i$ (Bastankhah and Porté-Agel, 2014). Other empirical expressions can be used, but this does not impact the validation process as both analytical and numerical approaches use σ regardless of how it is defined.

Figure 2 shows the lateral variation of the rotor-averaged wind speed deficit ($\tilde{W}$) normalised by the streamwise scaling function C at different downstream locations for the cases summarised above as calculated numerically (markers) and analytically (solid curves) using Eq. 13 for different values of the angle δ. The corresponding value of the eccentricity ξ, the veer coefficient ω, the ratio R/σ, and the parameter $\kappa = R^2/(6\sigma_{\text{ns}}^2)$ are indicated for each case. During the derivation of Eq. 13, the quantity κ was assumed to be small enough ($\lesssim 1$) to employ the approximation $I_\nu\left(\eta^2 R^2/(2\sigma_{\text{ns}}^2)\right) \sim (\eta^2 R^2/(4\sigma_{\text{ns}}^2))^\nu/\nu!$ (Appendix C). The listed values of κ in Fig. 2 verify this simplifying assumption as the maximum value of κ was approximately 0.35 which occurred 10 diameters downstream of the wake source for the low C_t and low T_i case (Fig. 2d). For the other cases, κ has even smaller values.

The comparison against the numerical evaluation of the rotor-averaged deficit indicates excellent accuracy of Eq. 13, even far downstream of the wake source ($x/D = 10$), where the wake is highly sheared by wind veer. At zero lateral offset between the

https://doi.org/10.5194/wes-2024-107
Preprint. Discussion started: 10 September 2024
© Author(s) 2024. CC BY 4.0 License.

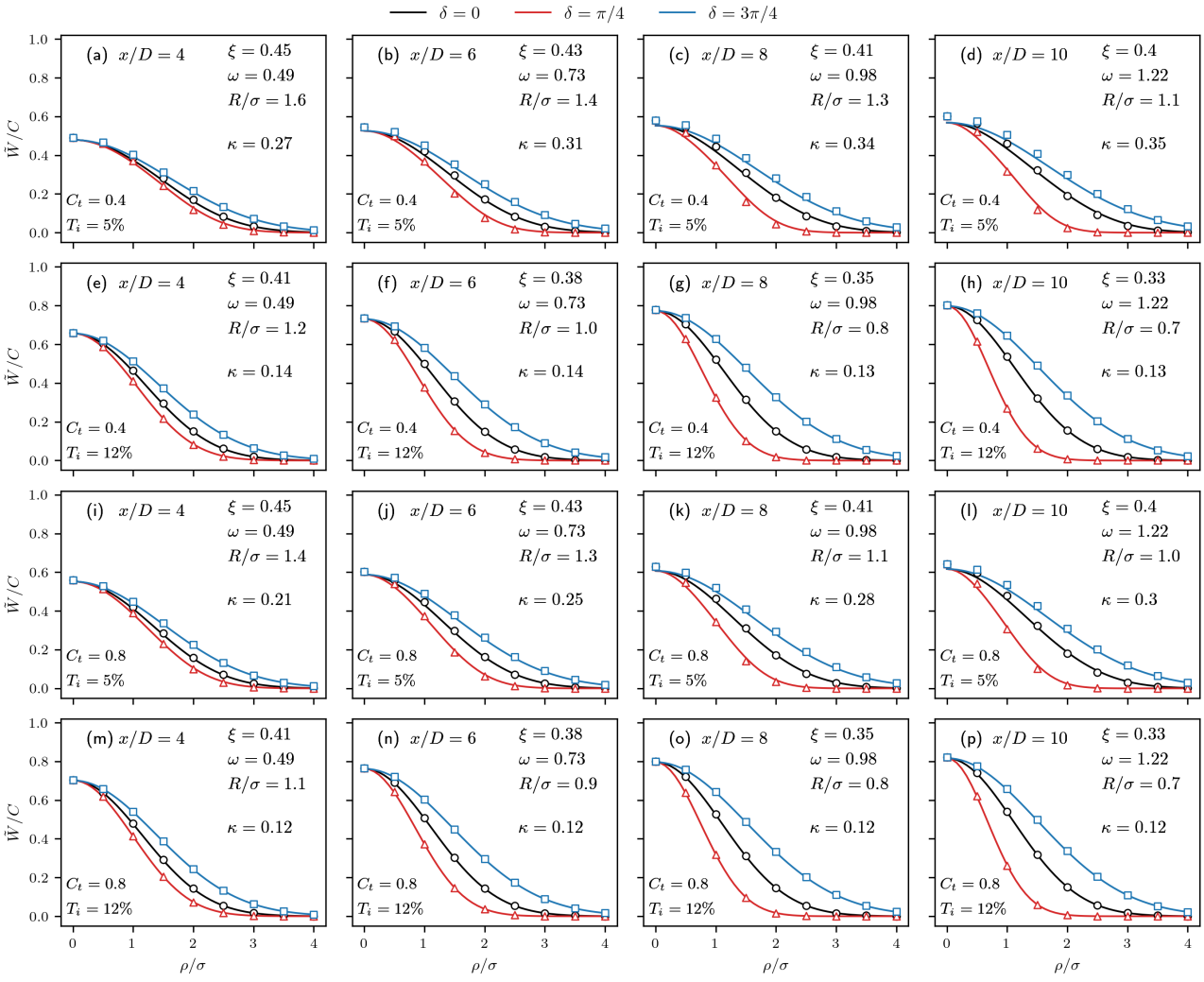

Figure 2. Normalised rotor-averaged deficit ($\tilde{W}/C$) calculated numerically (markers) using the set of discrete points shown in Fig. E1 and analytically (solid curves) using Eq. 13 for different values of the lateral offset ρ (normalised by the wake standard deviation σ) between the wake source and considered turbine. Each column represents a specific distance downstream of the wake source, and each row corresponds to a different combination of the thrust coefficient (C_t) of the upstream turbine and the free-stream turbulence intensity (T_i) as indicated. Indicated for each case are the wind-veer coefficient $\omega \approx 0.122\,x/D$ corresponding to a 7° difference in wind direction between the top and bottom tips of the upstream turbine, the eccentricity of the wake elliptic contour ξ due to a 20° yawing of the upstream turbine (Eq. 3), and the ratio of the radius of the considered turbine to the wake standard deviation R/σ (σ is obtained from Eq. 2). For each case, three values of the angle δ, which is the angle between the wake center and the center of the considered turbine (Fig. 1), are considered: 0, $\pi/4$, and $3\pi/4$. The quantity $\kappa = R^2/(6\sigma_{\rm ns}^2)$, which was assumed small in the derivation of Eq. 13 is recorded for each case as a validation to this simplifying assumption.

https://doi.org/10.5194/wes-2024-107
Preprint. Discussion started: 10 September 2024
© Author(s) 2024. CC BY 4.0 License.

considered turbine and the wake source ($\rho = 0$), the agreement between Eq. 13 and the numerical solution in Fig. 2 for all the shown cases indicates that the assumption of minimal impact of wake shearing and stretching on the wake center was justifiable, even at high values of the veer coefficient ω at $x/D = 10$. As the stretching and shearing of the wake shape due to wind-veer effects increase downstream of the wake source (ω increases with x/D), the role of the angle δ (hub-height difference) becomes more profound compared to locations close to wake source (first column vs last column in Fig. 2). Specifically, the low C_t and low T_i case is characterised by a slow rate of wake expansion (σ is smaller than the other cases), resulting in the largest deviation between the numerical and analytical solutions far downstream of the wake source (Fig. 2d), because the parameter κ is relatively larger. However, at large distances downstream of the wake source ($x/D \sim 10$) the magnitude of the wind-speed deficit is sufficiently small (the scaling function C is small) making any differences between the numerical and analytical solutions insignificant.

3.2 Multiple upstream wakes

So far, we examined the developed analytical solution for a single upstream wake, but a wind turbine is typically impacted by multiple upstream turbines, for which wake superposition models are applied. When the rotor-averaged deficit due to multiple upstream wakes is calculated numerically using a set of discrete points on its rotor disk, wake superposition of all upstream wakes is applied for each point on the rotor disk independently, followed by rotor averaging of the superposed deficits. Alternatively, the presented analytical solution (Eq. 13) corresponds to evaluating the rotor-averaged deficit for each upstream wake independently, followed by superposition of the rotor-averaged deficits. The impact of the order of applying wake superposition and rotor averaging depends on the structure of the superposition expression. Ali et al. (2024a) showed that for axisymmetric wakes the order of wake superposition and rotor averaging has no significant impact on the overall rotor-averaged deficit for both linear superposition (Niayifar and Porté-Agel, 2015) and root-mean-squared superposition (Voutsinas et al., 1990), and demonstrated this by application to the Horns Rev wind farm. In this section, we extend this analysis to the case of non-axisymmetric wakes to quantify the impact of the order of wake superposition and rotor averaging.

Expanding on the application presented by Ali et al. (2024a), we consider the Horns Rev wind farm but with yawed turbines to demonstrate the accuracy of Eq. 13 when combined with various wake superposition models against numerical approaches. The yaw angle of each turbine was obtained from the yaw optimisation study by Zhang et al. (2024) for a free stream flowing from West to East with a wind speed 8 ms^{-1} and a turbulence intensity of 7.7%. The employed row-averaged yaw angles are shown in Fig. 3a, along with a schematic of the farm's layout and the direction of the wind relative to the farm. We use the wake deflection model of Bastankhah and Porté-Agel (2016), and the turbine-induced turbulence model of Crespo and Hernandez (1996). The wake of each turbine is assumed to be Gaussian similar to the form in Eq. 1. No wind-veer effects are included in this comparison, and hence $\omega = 0$.

We consider three wake superposition models: linear superposition (Niayifar and Porté-Agel, 2015), root-mean-squared superposition (Voutsinas et al., 1990, hereafter RMS), and the product-based superposition model of Lanzilao and Meyers

https://doi.org/10.5194/wes-2024-107
Preprint. Discussion started: 10 September 2024
© Author(s) 2024. CC BY 4.0 License.

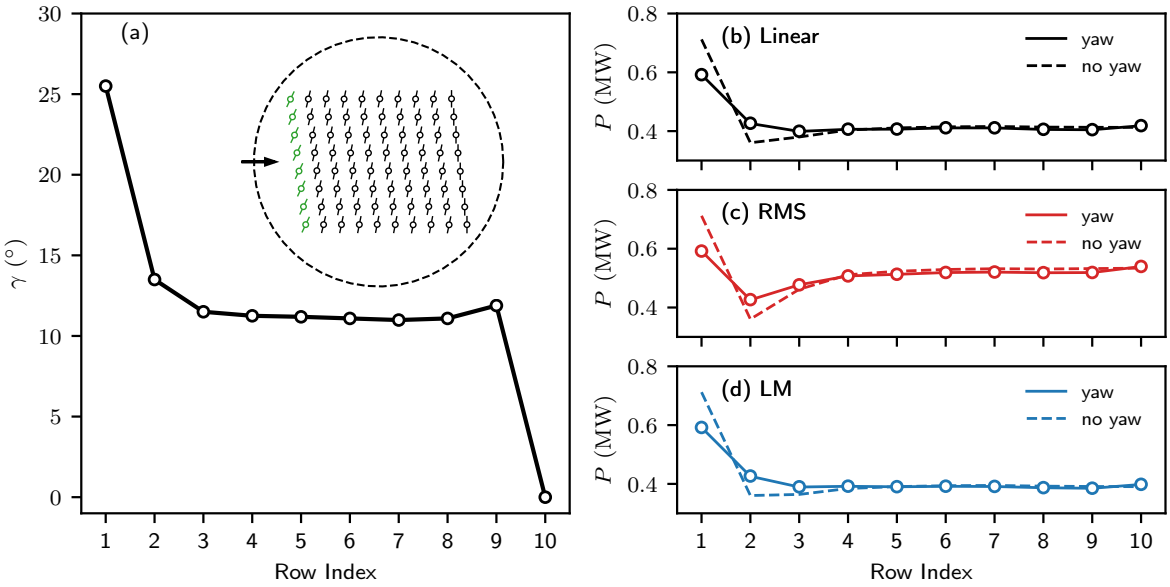

Figure 3. (a) The row-averaged yaw angle of the Horns Rev wind farm with respect to the free-stream wind from West to East (Zhang et al., 2024). Inset shows a schematic of the farm's layout where the yaw of each turbine is indicated and the first row is highlighted in green to indicate row definition. (b) The row-averaged power generation of the Horns Rev wind farm using linear wake superposition (Niayifar and Porté-Agel, 2015) obtained using the analytical solution of Eq. 13 (solid curve) compared to the numerical solution using the averaging points shown in Fig. E1 (markers). For reference, the case with no turbine yaw is shown by the dashed curve. The free-stream wind speed is $8\,\mathrm{m\,s^{-1}}$ and the free-stream turbulence intensity is 7.7%. (c) same as in sub-figure b but for the root-mean-squared superposition (Voutsinas et al., 1990). (d) same as in sub-figure b but for the product-based wake superposition of Lanzilao and Meyers (2022).

(2022, hereafter LM), which are defined as

$$\tilde{W}_{\mathrm{lin}} = \frac{1}{U_\infty}\sum_{j\in S}\tilde{u}_j W_j, \quad \tilde{W}_{\mathrm{RMS}} = \frac{1}{U_\infty}\sqrt{\sum_{j\in S}\tilde{u}_j^2 W_j^2}, \quad \text{and} \quad \tilde{W}_{\mathrm{LM}} = 1 - \prod_{j\in S}(1-W_j), \tag{14}$$

where U_∞ is the free-stream wind speed, and S is the set of all upstream turbines whose wakes influence the considered turbine. Figures 3b–d show the row-averaged power generation of the Horns Rev wind farm as calculated analytically (solid curves) and numerically (markers) for linear superposition (Fig. 3b), root-mean-squared superposition (Fig. 3c), and product-based superposition (Fig. 3d). The change in row-averaged power generation due to turbine yaw exhibits similar trends to that predicted by Zhang et al. (2024) with a reduction in power from the first row, a power uplift from the second and third rows, and only small variations (of order 1–2%) for subsequent rows (Figs. 3b–d). This is observed for the three considered wake superposition models, and power generation of later rows (third row and onwards) are more sensitive to the used superposition model than to the imposed yaw. The comparisons in Figs. 3b–d show that the analytical and numerical calculations of the row-averaged power generation are indistinguishable, indicating that the order of applying wake superposition and rotor averaging

https://doi.org/10.5194/wes-2024-107
Preprint. Discussion started: 10 September 2024
© Author(s) 2024. CC BY 4.0 License.

does not impact the accuracy of Eq. 13, which can be used with the considered wake superposition models as well as any superposition model that uses similar operators (i.e., linear, root-mean-squared, or product).

4 Discussion

In the current study, we derived and validated an expression for the surface integration of a non-axisymmetric Gaussian wake over a circular disk, depicting the rotor of a turbine whose rotor-averaged deficit is sought. The general integrated wake profile took into consideration wake stretching arising from the yawing of upstream turbines, and wake planar shearing due to wind-veer effects through a set of controlling variables: σ, ρ, δ, ξ, and ω, whose definitions were discussed in detail in section 2.1. The presented solution is compatible with any wake deflection model from the literature as all distances were referenced to the wake center. Alternatively, if the center of the upstream turbine is sought to be the reference location, then the definitions of ρ and δ need modifications to account for the wake horizontal deflection d. In this case, the modified lateral offset ρ^*, and the modified angle δ^* measured from the center of the upstream turbine are

$$\rho^* = \rho\sqrt{1+2\left(\frac{d}{\rho}\right)\cos\delta+\left(\frac{d}{\rho}\right)^2}, \quad \text{and} \quad \tan\delta^* = \frac{\sin\delta}{d/\rho+\cos\delta}. \tag{15}$$

The rotor-averaged deficit proposed in section 2.2 (Eq. 13) corresponds to a single upstream wake, whereas an operational wind turbine is typically impacted by multiple upstream wakes whose deficits are superposed using a variety of wake superposition models (e.g., Lissaman, 1979; Voutsinas et al., 1990). In a numerical framework that relies on a set of discrete points generated on the rotor disk of the considered turbine to calculate the rotor-averaged deficit, wake superposition due to all upstream wakes is applied to each point independently followed by a rotor averaging for the superposed wakes. Conversely, application of Eq. 13 to a turbine subject to multiple upstream wakes requires the evaluation of the rotor-averaged deficit for each wake followed by a superposition of these deficits. For a superposition model that relies on a linear operator to combine upstream deficits (e.g., Lissaman, 1979; Niayifar and Porté-Agel, 2015; Zong and Porté-Agel, 2021; Dar and Porté-Agel, 2024), the numerical and analytical approaches discussed above are the same, meaning that the order of applying wake superposition and rotor averaging has no effect. However, other wake superposition models rely on root-mean-squared operators (e.g., Katic et al., 1987; Voutsinas et al., 1990) for which the order of wake superposition and rotor averaging is not trivial. Ali et al. (2024a) showed mathematically that for a column of turbines of the same hub-height ($\delta = 0$) with no lateral offset ($\rho = 0$) where the wake of each turbine is axisymmetric ($\xi = \omega = 0$), the order in which wake superposition and rotor averaging calculations are applied results in insignificant differences as long as the number of upstream turbines with non-negligible deficits acting on the considered turbine is not large. They showed that for an analytical approach (rotor-averaging followed by superposition), the rotor-averaged deficit of the considered turbine is proportional to $e^{-1/(4\tilde{\sigma}^2)}$, where $\tilde{\sigma}$ is an averaged wake standard deviation for all the upstream turbines impacting the considered turbine, whereas for a numerical approach (superposition followed by rotor-averaging), the rotor-averaged deficit is proportional to $e^{-2/(9\tilde{\sigma}^2)}$. In a typical wind farm, the number of upstream turbines with non-negligible deficits acting on a turbine is 2–3 where one of these turbines has the dominant wake effect, making these two exponents very close. This conclusion naturally extends to the considered case of a non-axisymmetric

https://doi.org/10.5194/wes-2024-107
Preprint. Discussion started: 10 September 2024
© Author(s) 2024. CC BY 4.0 License.

wake, as the non-axisymmetric solution was shown to be a perturbation to a scaled axisymmetric solution (Eq. 13). Application to the Horns Rev wind farm showed that the numerical and analytical approaches using root-mean-squared superposition gave indistinguishable results (Fig. 3c).

The superposition model of Lanzilao and Meyers (2022) does not use linear nor root-mean-squared operators, but rather the product of the normalised rotor-averaged wind speeds of all upstream wake sources. We show in Appendix F that for this superposition model, and for any other superposition model of a similar operator, the numerical and analytical approaches are asymptotically identical if the upstream wakes of the considered turbine are assumed to operate independently. This assumption is justified as each turbine can be yawed independently of the other turbines depending on its onset wind, though such a strategy is not optimal for the whole wind farm performance. We also demonstrate that for small-enough upstream deficits ($W \lesssim 0.3$), the superposition model of Lanzilao and Meyers (2022) converges to a non-weighted linear superposition model, which explains the closeness in the estimated power generation by the two wake superposition models when applied to the Horns Rev wind farm (Figs. 3b, d). Similar to root-mean-squared superposition, when this product-based superposition model was applied to the Horns Rev wind farm, there were no distinguishable differences between the analytical and numerical solutions (Fig. 3d).

Some limitations should, however, be considered. The rotor-averaging process inherently assumes that a zero-deficit point on the rotor disk has a wind speed that is equal to that of the upstream turbine (wake source), rather than the free-stream wind speed or another background wind speed. This is referred to as partial waking of a turbine. Such an effect can be profound in the case of highly heterogeneous flow within a wind farm (e.g., in the case of extreme weather conditions such as hurricanes or in the case of extremely large wind farms). In such a scenario, both the numerical and analytical approaches based on engineering wake models have shortcomings as the underlying assumptions of the wake-deficit model cannot predict the interactions between the wakes and the heterogeneous background flow, which can lead to inaccurate wind speeds of the unwaked regions of a rotor.

The obtained expression for the rotor-averaged deficit was derived assuming that the considered turbine is normal to the free-stream flow, making the parameters σ, ξ, ω, and C constants across the rotor disk. If the considered turbine is yawed, these parameters are no longer constants but vary along the streamwise extents of the considered yawed turbine. These variations are small for a small yaw angle γ and are typically ignored, as the integration over a circle normal to the free-stream flow is approximately similar to that across an inclined ellipse extending from $x_o - R\sin\gamma$ to $x_o + R\sin\gamma$, where x_o is the streamwise coordinate of the center of the yawed turbine. Moreover, a yawed turbine experiences transverse wind whose magnitude is typically much smaller than the streamwise wind speed (Martínez-Tossas et al., 2019). This transverse wind is not included in Eq. 13 and needs to be modelled numerically, if required. Nonetheless, since the streamwise wind speed is dominant for small yaw angles and typical inter-turbine spacing, Eq. 13 presents a fast point-free expression that can be used even if the considered turbine has a small yaw angle.

Importantly, Eq. 13 is differentiable. Although not addressed in this study, Eq. 13 allows for obtaining mathematical expressions for the gradients of the rotor-averaged wind speed of a turbine with respect to its location in a farm and/or to the

https://doi.org/10.5194/wes-2024-107
Preprint. Discussion started: 10 September 2024
© Author(s) 2024. CC BY 4.0 License.

operating point of upstream turbines. This offers the potential to replace the heuristic search for global minima that is required for optimisation problems to a problem of obtaining the zeros of a set of non-linear equations.

5 Summary

An analytical expression for the rotor-averaged wind-speed deficit of a turbine operating within a Gaussian wake was derived and validated for a general lateral offset and hub-height difference between the wake source and the considered turbine. The Gaussian wake included wake stretching effects due to the yawing of the wake source as well as the planar shearing of the wake shape due to wind-veer effects. The presented expression was validated against numerical evaluation of the rotor-averaged deficit indicating excellent agreement at various downstream distances of the wake source, and at different combinations of the thrust coefficient of the wake source and the free-stream turbulence intensity. The expression of the rotor-averaged deficit for a single turbine wake can be applied to multiple wakes using any available superposition model that rely on linear operators, root-mean-squared operators or product operators as demonstrated by application to the Horns Rev wind farm. The expression for the rotor-averaged deficit is differentiable and can lay the ground for obtaining mathematical expressions for the gradients of the rotor-averaged deficit, and hence power production, with respect to a turbine's location and/or the operating conditions of upstream turbines, which can be beneficial for optimisation-based applications.

Code availability. A Python implementation of the presented analytical expression for the rotor-averaged deficit (Eq. 13) is publicly available from Ali et al. (2024b). The Python script used to generate Fig. 2 is also available in the same repository.

Appendix A

In this appendix, we show how Eq. 4 can be transferred from the wake axes y_n–z_n to the axes of the considered turbine y–z. From Eq. 4 along with the relation between the y_n–z_n and y–z axes (Fig. 1): $y_n = y + \Delta_y$ and $z_n = z + \Delta_z$, we have

$$\tilde{W} = \frac{C}{\pi R^2} \int_0^R \int_0^{2\pi} r e^{-(y+\Delta_y+\omega(z+\Delta_z))^2/(2\sigma_y^2)} e^{-(z+\Delta_z)^2/(2\sigma_z^2)} \, d\theta \, dr, \tag{A1}$$

By expanding the brackets in Eq. A1, the exponent can be written as $e^{-r^2 c_{r^2}/2} e^{-r\rho c_{r\rho}} e^{-\rho^2 c_{\rho^2}/2}$, where c_{r^2}, $c_{r\rho}$, and c_{ρ^2} are coefficients of r^2, $r\rho$, and ρ^2, respectively. Using $\langle y, z\rangle = r\langle \cos\theta, \sin\theta\rangle$ and $\langle \Delta_y, \Delta_z\rangle = \rho\langle \cos\delta, \sin\delta\rangle$, where $\langle t_1, t_2\rangle$ means t_1 or t_2, we have

$$c_{r^2} = \frac{\cos^2\theta}{\sigma_y^2} + \frac{\sin^2\theta}{\sigma_z^2} + \frac{\omega \sin 2\theta}{\sigma_y^2} + \frac{\omega^2 \sin^2\theta}{\sigma_y^2}, \tag{A2}$$

$$c_{r\rho} = \underbrace{\left(\frac{\omega \sin\delta + \cos\delta}{\sigma_y^2}\right)}_{a_1} \cos\theta + \underbrace{\left(\frac{1}{\sigma_z^2} + \omega\left(\frac{\omega \sin\delta + \cos\delta}{\sigma_y^2}\right)\right)}_{a_2} \sin\theta. \tag{A3}$$

https://doi.org/10.5194/wes-2024-107
Preprint. Discussion started: 10 September 2024
© Author(s) 2024. CC BY 4.0 License.

$$c_{\rho^2} = \frac{\cos^2\delta}{\sigma_y^2} + \frac{\sin^2\delta}{\sigma_z^2} + \frac{\omega\sin 2\delta}{\sigma_y^2} + \frac{\omega^2\sin^2\delta}{\sigma_y^2}. \tag{A4}$$

To simplify Eq. A2, we use the substitutions $\cos^2\theta = (1+\cos 2\theta)/2$ and $\sin^2\theta = (1-\cos 2\theta)/2$

$$c_{r^2} = \underbrace{\left(\frac{1}{2\sigma_y^2} + \frac{1}{2\sigma_z^2} + \frac{\omega^2}{2\sigma_y^2}\right)}_{1/\sigma_*^2} + \underbrace{\left(\frac{1}{2\sigma_y^2} - \frac{1}{2\sigma_z^2} - \frac{\omega^2}{2\sigma_y^2}\right)}_{1/\sigma_{**}^2}\cos 2\theta + \left(\frac{\omega}{\sigma_y^2}\right)\sin 2\theta, \tag{A5}$$

which can be further simplified by defining $1/\sigma_{\mathrm{ns}}^2 = \sqrt{1/\sigma_{**}^4 + \omega^2/\sigma_y^4}$ and $\tan\phi_{\mathrm{ns}} = \omega\sigma_{**}^2/\sigma_y^2$

$$c_{r^2} = \frac{1}{\sigma_*^2} + \frac{\cos(2\theta - \phi_{\mathrm{ns}})}{\sigma_{\mathrm{ns}}^2}. \tag{A6}$$

Using the same procedure and by replacing θ with δ, we have

$$c_{\rho^2} = \frac{1}{\sigma_*^2} + \frac{\cos(2\delta - \phi_{\mathrm{ns}})}{\sigma_{\mathrm{ns}}^2}. \tag{A7}$$

Finally, Eq. A3 can be simplified to

$$c_{r\rho} = \cos(\theta - \phi_{\mathrm{s}})/\sigma_{\mathrm{s}}^2, \tag{A8}$$

by defining $\sigma_{\mathrm{s}}^2 = 1/\sqrt{a_1^2 + a_2^2}$ and $\tan\phi_{\mathrm{s}} = a_2/a_1$, where a_1 and a_2 are defined in Eq. A3.

Appendix B

In this appendix, we present the solution to the integral M_θ in Eq. 5, which was based on a solution proposed by Gaidash (2023).

$$M_\theta = \frac{1}{\pi}\int_0^{2\pi} e^{-\eta^2 R^2\cos(2\theta-\phi_{\mathrm{ns}})/(2\sigma_{\mathrm{ns}}^2) - \eta R\rho\cos(\theta-\phi_{\mathrm{s}})/\sigma_{\mathrm{s}}^2}\, d\theta. \tag{B1}$$

Using the Jacobi–Anger expansion (Abramowitz and Stegun, 1972, 9.1.41–45; p. 361), we can write

$$e^{-\eta R\rho\cos(\theta-\phi_{\mathrm{s}})/\sigma_{\mathrm{s}}^2} = \sum_{\nu\in\mathbb{Z}}(-1)^\nu I_\nu\left(\frac{\eta R\rho}{\sigma_{\mathrm{s}}^2}\right) e^{i\nu(\theta-\phi_{\mathrm{ns}}/2)} e^{i\nu(\phi_{\mathrm{ns}}/2-\phi_{\mathrm{s}})}, \tag{B2}$$

where I_ν is the modified Bessel function of order ν, and $\mathbb{Z}$ is the set of integers. Using Eq. B2, the integral M_θ becomes

$$M_\theta = \frac{1}{\pi}\sum_{\nu\in\mathbb{Z}}(-1)^\nu e^{i\nu(\phi_{\mathrm{ns}}/2-\phi_{\mathrm{s}})} I_\nu\left(\frac{\eta R\rho}{\sigma_{\mathrm{s}}^2}\right)\int_0^{2\pi} e^{-\eta^2 R^2\cos(2\theta-\phi_{\mathrm{ns}})/(2\sigma_{\mathrm{ns}}^2)} e^{i\nu(\theta-\phi_{\mathrm{ns}}/2)}\, d\theta. \tag{B3}$$

The integral in Eq. B3 vanishes for odd values of ν. Also, since M_θ is real we can write

$$M_\theta = 2\sum_{\nu\in\mathbb{Z}}\cos(\nu(2\phi_{\mathrm{s}} - \phi_{\mathrm{ns}}))\, I_{2\nu}\left(\frac{\eta R\rho}{\sigma_{\mathrm{s}}^2}\right)\int_0^{\pi} e^{-\eta^2 R^2\cos(\theta'-\phi_{\mathrm{ns}})/2\sigma_{\mathrm{ns}}^2}\cos(\nu(\theta' - \phi_{\mathrm{ns}}))\, d\theta', \tag{B4}$$

https://doi.org/10.5194/wes-2024-107
Preprint. Discussion started: 10 September 2024
© Author(s) 2024. CC BY 4.0 License.

where $\theta' = 2\theta$. The integral in Eq. B4 can be solved using (Gradshteyn and Ryzhik, 2007, 3.915(2) p. 491)

$$\int_0^\pi e^{-t\cos\zeta}\cos(\nu\zeta)\,d\zeta = (-1)^\nu \pi I_\nu(t), \tag{B5}$$

which is insensitive to a phase shift ϕ_{ns}. Hence, M_θ becomes

$$M_\theta = 2\sum_{\nu\in\mathbb{Z}}(-1)^\nu \cos(\nu(2\phi_{\text{s}} - \phi_{\text{ns}}))\, I_{2\nu}\left(\frac{\eta R\rho}{\sigma_{\text{s}}^2}\right) I_\nu\left(\frac{\eta^2 R^2}{2\sigma_{\text{ns}}^2}\right), \tag{B6}$$

which can be further simplified using the fact that $I_{-\nu}(x) = I_\nu(x)$ for an integer ν

$$M_\theta = 2I_0\left(\frac{\eta R\rho}{\sigma_{\text{s}}^2}\right) I_0\left(\frac{\eta^2 R^2}{2\sigma_{\text{ns}}^2}\right) + 4\sum_{\nu\geq 1}(-1)^\nu \cos(\nu(2\phi_{\text{s}} - \phi_{\text{ns}}))\, I_{2\nu}\left(\frac{\eta R\rho}{\sigma_{\text{s}}^2}\right) I_\nu\left(\frac{\eta^2 R^2}{2\sigma_{\text{ns}}^2}\right). \tag{B7}$$

Appendix C

In this appendix, we provide a solution to the integral M_η defined in Eq. 5 along with solution of the integral M_θ (Eq. 7) which was detailed in Appendix B

$$M_\eta = 2\int_0^1 \eta e^{-\eta^2 R^2/(2\sigma_*^2)} I_0\left(\frac{\eta R\rho}{\sigma_{\text{s}}^2}\right) I_0\left(\frac{\eta^2 R^2}{2\sigma_{\text{ns}}^2}\right)\, d\eta + 4\sum_{\nu\geq 1}(-1)^\nu \cos(\nu\phi)\int_0^1 \eta e^{-\eta^2 R^2/(2\sigma_*^2)} I_{2\nu}\left(\frac{\eta R\rho}{\sigma_{\text{s}}^2}\right) I_\nu\left(\frac{\eta^2 R^2}{2\sigma_{\text{ns}}^2}\right)\, d\eta \tag{C1}$$

The argument of the terms in the form $I_\nu\left(\eta^2 R^2/(2\sigma_{\text{ns}}^2)\right)$ is sufficiently small ($\lesssim 1$) for the ranges outlined in section 2.1 with an average value of $\kappa = R^2/(6\sigma_{\text{ns}}^2)$ for $0 \leq \eta \leq 1$. Hence, we employ the approximation $I_\nu\left(\eta^2 R^2/(2\sigma_{\text{ns}}^2)\right) \sim (\eta^2 R^2/(4\sigma_{\text{ns}}^2))^\nu/\nu!$ (Abramowitz and Stegun, 1972, 9.6.7; p. 375). The integral M_η becomes

$$M_\eta \approx 2\mu_0 + 4\sum_{\nu\geq 1}\frac{1}{\nu!}\left(\frac{-R^2}{4\sigma_{\text{ns}}^2}\right)^\nu \cos(\nu\phi)\underbrace{\int_0^1 \eta^{1+2\nu} e^{-\eta^2 R^2/(2\sigma_*^2)} I_{2\nu}\left(\frac{\eta R\rho}{\sigma_{\text{s}}^2}\right)\, d\eta}_{\Lambda_{2\nu}}, \tag{C2}$$

where

$$\mu_0 = \int_0^1 \eta e^{-\eta^2 R^2/(2\sigma_*^2)} I_0\left(\frac{\eta R\rho}{\sigma_{\text{s}}^2}\right)\, d\eta. \tag{C3}$$

Solving the integral μ_0 is discussed in more detail in section 2.2. The solution to the integrals $\Lambda_{2\nu}$ is derived in detail in Appendix D.

$$\Lambda_{2\nu} = \left(\frac{\rho\sigma_*^2}{R\sigma_{\text{s}}^2}\right)^{2\nu}\left[\mu_0 - \frac{\sigma_*^2}{R^2}e^{-R^2/(2\sigma_*^2)}\sum_{k=1}^{2\nu}\left(\frac{\rho\sigma_*^2}{R\sigma_{\text{s}}^2}\right)^{-k} I_k\left(\frac{R\rho}{\sigma_{\text{s}}^2}\right)\right] \tag{C4}$$

https://doi.org/10.5194/wes-2024-107
Preprint. Discussion started: 10 September 2024
© Author(s) 2024. CC BY 4.0 License.

Therefore, M_η becomes

$$M_\eta \approx 2\mu_0 \left(1 + 2\sum_{\nu\geq 1} \frac{(-\chi_{\rm ns}^2)^\nu \cos(\nu\phi)}{\nu!}\right) - \frac{4\sigma_*^2}{R^2} e^{-R^2/(2\sigma_*^2)} \sum_{\nu\geq 1} \frac{(-\chi_{\rm ns}^2)^\nu \cos(\nu\phi)}{\nu!} \left[\sum_{k=1}^{2\nu} \left(\frac{\rho\sigma_*^2}{R\sigma_{\rm s}^2}\right)^{-k} I_k\left(\frac{R\rho}{\sigma_{\rm s}^2}\right)\right], \tag{C5}$$

where $\chi_{\rm ns} = \rho\sigma_*^2/(2\sigma_{\rm ns}\sigma_{\rm s}^2)$. For the sum over ν, we have

$$\mathcal{P}_{\rm ns} = \sum_{\nu\geq 1} \frac{(-\chi_{\rm ns}^2)^\nu \cos(\nu\phi)}{\nu!} = e^{-\chi_{\rm ns}^2 \cos\phi} \cos(\chi_{\rm ns}^2 \sin\phi) - 1. \tag{C6}$$

Also, the modified Bessel function $I_\nu(x)$ decays rapidly with ν, and hence we only keep the terms with $\nu \leq 2$ in the right-hand side of Eq. C5. Therefore, Eq. C5 simplifies to

$$M_\eta \approx 2\mu_0 (1 + 2\mathcal{P}_{\rm ns}) - \frac{4\sigma_*^2}{R^2} e^{-R^2/(2\sigma_*^2)} \mathcal{P}_{\rm ns} \left[\frac{\lambda}{\rho} I_1\left(\frac{R\rho}{\sigma_{\rm s}^2}\right) + \frac{\lambda^2}{\rho^2} I_2\left(\frac{R\rho}{\sigma_{\rm s}^2}\right)\right]. \tag{C7}$$

where $\lambda = R\sigma_{\rm s}^2/\sigma_*^2$.

Appendix D

In this appendix, we present a solution to a generic integral in the form

$$\Lambda_\nu(\beta,\vartheta) = \int_0^1 \eta^{1+\nu} e^{-\eta^2\beta^2/2} I_\nu(\eta\vartheta)\, d\eta, \tag{D1}$$

where ν is an integer, and β and ϑ are constants. To evaluate Λ_ν we employ $\partial/\partial\eta\,(\eta^\nu I_\nu(\eta\vartheta)) = \vartheta\eta^\nu I_{\nu-1}(\eta\vartheta)$. Integrating Eq. D1 by parts leads to the recursion

$$\Lambda_\nu(\beta,\vartheta) = -\frac{e^{-\beta^2/2}}{\beta^2} I_\nu(\vartheta) + \frac{\vartheta}{\beta^2}\Lambda_{\nu-1}(\beta,\vartheta), \tag{D2}$$

which can be solved using the generating function $\mathcal{F}(\eta) = \sum_{\nu\geq 1} \Lambda_\nu \eta^\nu$. Multiplying Eq. D2 by η^ν and summing over ν gives

$$\sum_{\nu\geq 1} \Lambda_\nu \eta^\nu = -\frac{e^{-\beta^2/2}}{\beta^2} \sum_{\nu\geq 1} I_\nu(\vartheta)\eta^\nu + \frac{\vartheta}{\beta^2} \sum_{\nu\geq 1} \Lambda_{\nu-1}\eta^\nu, \tag{D3}$$

which simplifies into

$$\mathcal{F}(\eta) = -\frac{e^{-\beta^2/2}}{\beta^2} \sum_{\nu\geq 1} I_\nu(\vartheta)\eta^\nu + \frac{\vartheta\eta}{\beta^2}(\Lambda_0 + \mathcal{F}(\eta)). \tag{D4}$$

Solving Eq. D4 for $\mathcal{F}(\eta)$ and using Taylor's expansion $(1 - \vartheta\eta/\beta^2)^{-1} = \sum_{m\geq 0} (\vartheta\eta/\beta^2)^m$

$$\mathcal{F}(\eta) = -\frac{e^{-\beta^2/2}}{\beta^2} \sum_{\nu\geq 1}\sum_{m\geq 0} \left(\frac{\vartheta}{\beta^2}\right)^m I_\nu(\vartheta)\eta^{\nu+m} + \Lambda_0 \sum_{m\geq 0} \left(\frac{\vartheta\eta}{\beta^2}\right)^{m+1}. \tag{D5}$$

https://doi.org/10.5194/wes-2024-107
Preprint. Discussion started: 10 September 2024
© Author(s) 2024. CC BY 4.0 License.

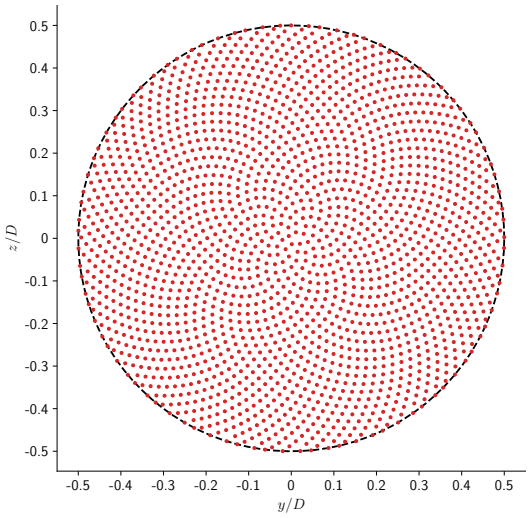

Figure E1. A uniform sunflower distribution of 2000 points over the surface a circle to be used to numerically evaluate the rotor-averaged deficit due to an upstream wake in the form of Eq. 1 and provide a reference to validate Eq. 13. More details on this distribution is available in Appendix E.

Finally, the integral Λ_ν is the coefficient of η^ν in Eq. D5

$$\Lambda_\nu(\beta,\vartheta) = \left(\frac{\vartheta}{\beta^2}\right)^\nu \left[\Lambda_0(\beta,\vartheta) - \frac{e^{-\beta^2/2}}{\beta^2}\sum_{k=1}^{\nu}\left(\frac{\vartheta}{\beta^2}\right)^{-k} I_k(\vartheta)\right], \tag{D6}$$

where $\Lambda_0(\beta,\vartheta)$ is

$$\Lambda_0(\beta,\vartheta) = \int_0^1 \eta e^{-\eta^2\beta^2/2} I_0(\eta\vartheta)\, d\eta. \tag{D7}$$

Appendix E

In this appendix, the sunflower distribution of points across a circle is summarised. The polar coordinates r_k and θ_k of a point of index k (out of N total points) on a circle of radius R are defined as

$$r_k = \begin{cases} R & \text{if } k > N-b \\ R\sqrt{\frac{k-1/2}{N-(b+1)/2}} & \text{otherwise} \end{cases} \tag{E1}$$

$$\theta_k = \frac{2\pi k}{\varphi^2}, \tag{E2}$$

https://doi.org/10.5194/wes-2024-107
Preprint. Discussion started: 10 September 2024
© Author(s) 2024. CC BY 4.0 License.

where $\varphi = (\sqrt{5}+1)/2$ is the golden ratio, and the constant $b = \text{round}(2\sqrt{N})$ with the function "round" returning the nearest integer. The resulting distribution of points is shown in Fig. E1. An implementation of this distribution can be found in Ali et al. (2024b).

Appendix F

In this appendix, we examine the effect of the order of applying wake superposition and the rotor averaging for the product-based wake superposition model of Lanzilao and Meyers (2022). Consider a wind turbine impacted by a set S of upstream wakes. Assuming a set of N discrete points on the rotor disk of the considered turbine, the numerical approach (wake superposition followed by rotor averaging) of obtaining the rotor-averaged deficit is

$$^{\text{LM}}\tilde{W}_{\text{num}} = \frac{1}{N}\sum_{k=1}^{N}\left(1 - \prod_{j\in S}(1 - W_j(k))\right), \tag{F1}$$

where $W_j(k)$ is the normalised wind-speed deficit of a point of index k on the rotor disk of the considered turbine due to the wake of an upstream turbine of index j. The product over the set S in Eq. F1 can be expanded as

$$\prod_{j\in S}(1 - W_j(k)) = 1 - \sum_{j\in S} W_j(k) + \sum_{\substack{i,j\in S\\ i\neq j}} W_i(k)W_j(k) + \mathcal{O}(W^3). \tag{F2}$$

We can neglect the higher order terms of W (order 3 and higher) compared to the lower order terms, and hence Eq. F1 simplifies to

$$^{\text{LM}}\tilde{W}_{\text{num}} \approx \sum_{j\in S}\left(\frac{1}{N}\sum_{k=1}^{N} W_j(k)\right) - \sum_{\substack{i,j\in S\\ i\neq j}}\left(\frac{1}{N}\sum_{k=1}^{N} W_i(k)W_j(k)\right). \tag{F3}$$

If the rotor averaging over a set of N points asymptotically approaches the analytical average, then

$$^{\text{LM}}\tilde{W}_{\text{num}} \simeq \sum_{j\in S}\tilde{W}_j - \sum_{\substack{i,j\in S\\ i\neq j}}\widetilde{W_iW_j}. \tag{F4}$$

Alternatively, the corresponding analytical approach (rotor averaging followed by wake superposition) of obtaining the rotor-averaged deficit is

$$^{\text{LM}}\tilde{W}_{\text{anl}} = 1 - \prod_{j\in S}\left(1 - \tilde{W}_j\right) \approx \sum_{j\in S}\tilde{W}_j - \sum_{\substack{i,j\in S\\ i\neq j}}\tilde{W}_i\tilde{W}_j. \tag{F5}$$

The difference between the numerical and analytical approaches originates from $\widetilde{W_iW_j}$ in Eq. F4 versus $\tilde{W}_i\tilde{W}_j$ in Eq. F5, where the difference between these two quantities acts as a covariance for the set of upstream deficits. If the mutual impacts between the upstream turbines are neglected by assuming the turbines operate almost independently (i.e., $\widetilde{W_iW_j} \sim \tilde{W}_i\tilde{W}_j$), then an asymptotic resemblance between $^{\text{LM}}\tilde{W}_{\text{num}}$ and $^{\text{LM}}\tilde{W}_{\text{anl}}$ is achieved. In the case of small-enough deficits, the superposition of Lanzilao and Meyers (2022) approaches a non-weighted linear superposition when $W^2 \ll W$.

https://doi.org/10.5194/wes-2024-107
Preprint. Discussion started: 10 September 2024
© Author(s) 2024. CC BY 4.0 License.

Author contributions. All the authors contributed to the conceptualisation of this study. KA derived the mathematical expressions and prepared the original draft of the manuscript, which was reviewed and edited by TS and PO. Funding acquisition and supervision was done by TS and PO.

Competing interests. The authors declare that they have no conflict of interest.

Financial support. This research was partly supported by the Supergen Offshore Renewable Energy hub, funded by the Engineering and Physical Science Research Council (EPSRC) grants no. EP/S000747/1 and EP/Y016297/1. The present work has been partly supported by the Dame Kathleen Ollerenshaw Fellowship that Dr Ouro holds at the University of Manchester.

https://doi.org/10.5194/wes-2024-107
Preprint. Discussion started: 10 September 2024
© Author(s) 2024. CC BY 4.0 License.

References

Abkar, M., Sørensen, J., and Porté-Agel, F.: An Analytical Model for the Effect of Vertical Wind Veer on Wind Turbine Wakes, Energies, 11, 1838, https://doi.org/10.3390/en11071838, 2018.

Abramowitz, M. and Stegun, I. A.: Handbook of Mathematical Functions with formulas, graphs, and mathematical tables, Dover Publications, 1972.

Ali, K., Schultz, D. M., Revell, A., Stallard, T., and Ouro, P.: Assessment of Five Wind-Farm Parameterizations in the Weather Research and Forecasting Model: A Case Study of Wind Farms in the North Sea, Monthly Weather Review, 151, 2333 – 2359, https://doi.org/10.1175/MWR-D-23-0006.1, 2023.

Ali, K., Stallard, T., and Ouro, P.: Evaluating wind-farm power generation using a new direct integration of axisymmetric turbine wake, Journal of Physics: Conference Series, 2767, 092 015, https://doi.org/10.1088/1742-6596/2767/9/092015, 2024a.

Ali, K., Stallard, T., and Ouro, P.: Analytical evaluation of non-axisymmetric Gaussian wind-turbine wake including yaw and wind-veer effects, https://doi.org/10.5281/zenodo.13272760, 2024b.

Ali, K., Stallard, T., and Ouro, P.: A diffusion-based wind turbine wake model, manuscript submitted for publication, 2024c.

Allaerts, D. and Meyers, J.: Sensitivity and feedback of wind-farm-induced gravity waves, Journal of Fluid Mechanics, 862, 990–1028, https://doi.org/10.1017/jfm.2018.969, 2019.

Bastankhah, M. and Porté-Agel, F.: A new analytical model for wind-turbine wakes, Renewable Energy, 70, 116–123, https://doi.org/10.1016/j.renene.2014.01.002, Special issue on aerodynamics of offshore wind energy systems and wakes, 2014.

Bastankhah, M. and Porté-Agel, F.: Experimental and theoretical study of wind turbine wakes in yawed conditions, Journal of Fluid Mechanics, 806, 506–541, https://doi.org/10.1017/jfm.2016.595, 2016.

Bay, C. J., Annoni, J., Taylor, T., Pao, L., and Johnson, K.: Active Power Control for Wind Farms Using Distributed Model Predictive Control and Nearest Neighbor Communication, in: 2018 Annual American Control Conference (ACC), pp. 682–687, https://doi.org/10.23919/ACC.2018.8431764, 2018.

Blondel, F. and Cathelain, M.: An alternative form of the super-Gaussian wind turbine wake model, Wind Energy Science, 5, 1225–1236, https://doi.org/10.5194/wes-5-1225-2020, 2020.

Cheng, W.-C. and Porté-Agel, F.: A Simple Physically-Based Model for Wind-Turbine Wake Growth in a Turbulent Boundary Layer, Boundary-Layer Meteorology, 169, 1–10, https://doi.org/10.1007/s10546-018-0366-2, 2018.

Crespo, A. and Hernandez, J.: Turbulence characteristics in wind-turbine wakes, Journal of Wind Engineering and Industrial Aerodynamics, 61, 71–85, https://doi.org/10.1016/0167-6105(95)00033-X, 1996.

Dar, A. S. and Porté-Agel, F.: Wind turbine wake superposition under pressure gradient, Physics of Fluids, 36, 015 145, https://doi.org/10.1063/5.0185542, 2024.

Fitch, A. C., Olson, J. B., Lundquist, J. K., Dudhia, J., Gupta, A. K., Michalakes, J., and Barstad, I.: Local and Mesoscale Impacts of Wind Farms as Parameterized in a Mesoscale NWP Model, Monthly Weather Review, 140, 3017 – 3038, https://doi.org/10.1175/MWR-D-11-00352.1, 2012.

Gaidash, T.: Integration of exponential of a function of cosines, Mathematics Stack Exchange, https://math.stackexchange.com/q/4760090, URL: https://math.stackexchange.com/q/4760090 (version: 2023-08-29), 2023.

Gao, L., Li, B., and Hong, J.: Effect of wind veer on wind turbine power generation, Physics of Fluids, 33, 015 101, https://doi.org/10.1063/5.0033826, 2021.

https://doi.org/10.5194/wes-2024-107
Preprint. Discussion started: 10 September 2024
© Author(s) 2024. CC BY 4.0 License.

Gradshteyn, I. and Ryzhik, I.: 3–4 - Definite Integrals of Elementary Functions, in: Table of Integrals, Series, and Products, edited by Jeffrey, A., Zwillinger, D., Gradshteyn, I., and Ryzhik, I., pp. 247–617, Academic Press, Boston, 7 edn., ISBN 978-0-12-373637-6, https://doi.org/10.1016/B978-0-08-047111-2.50013-3, 2007.

Holoborodko, P.: Cubature formulas for the unit disk, http://www.holoborodko.com/pavel/numerical-methods/numerical-integration/cubature-formulas-for-the-unit-disk/, 2011.

Hou, P., Hu, W., Chen, C., Soltani, M., and Chen, Z.: Optimization of offshore wind farm layout in restricted zones, Energy, 113, 487–496, https://doi.org/10.1016/j.energy.2016.07.062, 2016.

Jensen, N.: A note on wind generator interaction, no. 2411 in Risø-M, Risø National Laboratory, ISBN 87-550-0971-9, 1983.

Katic, I., Højstrup, J., and Jensen, N.: A Simple Model for Cluster Efficiency, in: EWEC'86. Proceedings. Vol. 1, edited by Palz, W. and Sesto, E., pp. 407–410, A. Raguzzi, european Wind Energy Association Conference and Exhibition, EWEC '86 ; Conference date: 06-10-1986 Through 08-10-1986, 1987.

Keane, A., Aguirre, P. E. O., Ferchland, H., Clive, P., and Gallacher, D.: An analytical model for a full wind turbine wake, Journal of Physics: Conference Series, 753, 032 039, https://doi.org/10.1088/1742-6596/753/3/032039, 2016.

Lanzilao, L. and Meyers, J.: A new wake-merging method for wind-farm power prediction in the presence of heterogeneous background velocity fields, Wind Energy, 25, 237–259, https://doi.org/10.1002/we.2669, 2022.

Li, B., He, J., Ge, M., Ma, H., Du, B., Yang, H., and Liu, Y.: Study of three wake control strategies for power maximization of offshore wind farms with different layouts, Energy Conversion and Management, 268, 116 059, https://doi.org/10.1016/j.enconman.2022.116059, 2022.

Ling, Z., Zhao, Z., Liu, Y., Liu, H., Ali, K., Liu, Y., Wen, Y., Wang, D., Li, S., and Su, C.: Multi-objective layout optimization for wind farms based on non-uniformly distributed turbulence and a new three-dimensional multiple wake model, Renewable Energy, 227, 120 558, https://doi.org/10.1016/j.renene.2024.120558, 2024.

Lissaman, P. B. S.: Energy Effectiveness of Arbitrary Arrays of Wind Turbines, Journal of Energy, 3, 323–328, https://doi.org/10.2514/3.62441, 1979.

Maas, O. and Raasch, S.: Wake properties and power output of very large wind farms for different meteorological conditions and turbine spacings: a large-eddy simulation case study for the German Bight, Wind Energy Science, 7, 715–739, https://doi.org/10.5194/wes-7-715-2022, 2022.

Martínez-Tossas, L. A., Annoni, J., Fleming, P. A., and Churchfield, M. J.: The aerodynamics of the curled wake: a simplified model in view of flow control, Wind Energy Science, 4, 127–138, https://doi.org/10.5194/wes-4-127-2019, 2019.

Niayifar, A. and Porté-Agel, F.: A new analytical model for wind farm power prediction, Journal of Physics: Conference Series, 625, 012 039, https://doi.org/10.1088/1742-6596/625/1/012039, 2015.

Ouro, P. and Lazennec, M.: Theoretical modelling of the three-dimensional wake of vertical axis turbines, Flow, 1, E3, https://doi.org/10.1017/flo.2021.4, 2021.

Qian, G.-W. and Ishihara, T.: A New Analytical Wake Model for Yawed Wind Turbines, Energies, 11, https://doi.org/10.3390/en11030665, 2018.

Rosenheinrich, W.: Tables of some indefinite integral of Bessel functions of integer order, Ernst - Abbe - Hochschule Jena, 2017.

Shapiro, C. R., Starke, G. M., and Gayme, D. F.: Turbulence and Control of Wind Farms, Annual Review of Control, Robotics, and Autonomous Systems, 5, 579–602, https://doi.org/10.1146/annurev-control-070221-114032, 2022.

Snaiki, R. and Makki, S.: A new analytical wind turbine wake model considering the effects of coriolis force and yawed conditions, Journal of Wind Engineering and Industrial Aerodynamics, 250, 105 767, https://doi.org/10.1016/j.jweia.2024.105767, 2024.

https://doi.org/10.5194/wes-2024-107
Preprint. Discussion started: 10 September 2024
© Author(s) 2024. CC BY 4.0 License.

Stallard, T., Feng, T., and Stansby, P.: Experimental study of the mean wake of a tidal stream rotor in a shallow turbulent flow, Journal of Fluids and Structures, 54, 235–246, https://doi.org/10.1016/j.jfluidstructs.2014.10.017, 2015.

Stanley, A. P. J. and Ning, A.: Massive simplification of the wind farm layout optimization problem, Wind Energy Science, 4, 663–676, https://doi.org/10.5194/wes-4-663-2019, 2019.

Stipa, S., Ajay, A., Allaerts, D., and Brinkerhoff, J.: The multi-scale coupled model: a new framework capturing wind farm–atmosphere interaction and global blockage effects, Wind Energy Science, 9, 1123–1152, https://doi.org/10.5194/wes-9-1123-2024, 2024.

Veers, P., Bottasso, C. L., Manuel, L., Naughton, J., Pao, L., Paquette, J., Robertson, A., Robinson, M., Ananthan, S., Barlas, T., Bianchini, A., Bredmose, H., Horcas, S. G., Keller, J., Madsen, H. A., Manwell, J., Moriarty, P., Nolet, S., and Rinker, J.: Grand challenges in the design, manufacture, and operation of future wind turbine systems, Wind Energy Science, 8, 1071–1131, https://doi.org/10.5194/wes-8-1071-2023, 2023.

Voutsinas, S., Rados, K., and Zervos, A.: On the Analysis of Wake Effects in Wind Parks, Wind Engineering, 14, 204–219, http://www.jstor.org/stable/43749429, 1990.

Walter, K., Weiss, C. C., Swift, A. H. P., Chapman, J., and Kelley, N. D.: Speed and Direction Shear in the Stable Nocturnal Boundary Layer, Journal of Solar Energy Engineering, 131, 011 013, https://doi.org/10.1115/1.3035818, 2009.

Zhang, Z., Huang, P., Bitsuamlak, G., and Cao, S.: Analytical solutions for yawed wind-turbine wakes with application to wind-farm power optimization by active yaw control, Ocean Engineering, 304, 117 691, https://doi.org/10.1016/j.oceaneng.2024.117691, 2024.

Zong, H. and Porté-Agel, F.: Experimental investigation and analytical modelling of active yaw control for wind farm power optimization, Renewable Energy, 170, 1228–1244, https://doi.org/10.1016/j.renene.2021.02.059, 2021.